

Human contribution to the risk of 2021 northwestern Pacific concurrent marine and terrestrial summer heat

Article

Accepted Version

Tang, H., Wang, J., Chen, Y., Tett, S. F. B., Sun, Y., Cheng, L., Sparrow, S. and Dong, B. ORCID: <https://orcid.org/0000-0003-0809-7911> (2023) Human contribution to the risk of 2021 northwestern Pacific concurrent marine and terrestrial summer heat. *Bulletin of the American Meteorological Society*, 104 (3). E673-E679. ISSN 1520-0477 doi: 10.1175/BAMS-D-22-0238.1 Available at <https://centaur.reading.ac.uk/111426/>

It is advisable to refer to the publisher's version if you intend to cite from the work. See [Guidance on citing](#).

To link to this article DOI: <http://dx.doi.org/10.1175/BAMS-D-22-0238.1>

Publisher: American Meteorological Society

All outputs in CentAUR are protected by Intellectual Property Rights law, including copyright law. Copyright and IPR is retained by the creators or other copyright holders. Terms and conditions for use of this material are defined in the [End User Agreement](#).

www.reading.ac.uk/centaur

CentAUR

Central Archive at the University of Reading

Reading's research outputs online

**Human contribution to the risk of 2021 Northwestern Pacific
concurrent marine and terrestrial summer heat**

Haosu Tang^{1,7}, Jun Wang^{1*}, Yang Chen², Simon F. B. Tett³, Ying Sun⁴, Lijing Cheng¹,
Sarah Sparrow⁵, and Buwen Dong⁶

¹State Key Laboratory of Numerical Modeling for Atmospheric Sciences and Geophysical Fluid
Dynamics (LASG) / Key Laboratory of Regional Climate Environment for Temperate East Asia
(RCE-TEA) / International Center for Climate and Environment Sciences (ICCES), Institute of
Atmospheric Physics, Chinese Academy of Sciences, Beijing, China

²State Key Laboratory of Severe Weather, Chinese Academy of Meteorological Sciences, Beijing,
China

³School of Geosciences, University of Edinburgh, Edinburgh, UK

⁴National Climate Center, Laboratory for Climate Studies, China Meteorological
Administration, Beijing, China

⁵Oxford e-Research Centre, Department of Engineering Science, University of Oxford, Oxford,
UK

⁶National Centre for Atmospheric Science, Department of Meteorology, University of Reading,
Reading, UK

⁷University of Chinese Academy of Sciences, Beijing, China

*Correspondence to wangjun@tea.ac.cn

Capsule Summary: Current human-induced warming has led to approximately a 30-fold increase in the occurrence probability of 2021 Northwestern Pacific concurrent marine and terrestrial summer heat.

Introduction. July 2021 was the warmest month ever recorded for the globe, during which several extreme weather events occurred (NOAA, 2022). Less noticed but as important, an unprecedentedly intense marine heatwave impacted broad swaths of the Northwestern Pacific (NWP; black box in Fig. 1a; 150–180°E; 30–50°N), in the same month, with regional mean sea surface temperature anomalies (SSTA; relative to 1961–1990) up to 1.23°C (Kuroda and Setou 2021). This marine heat caused an unprecedented outbreak of red tides off Hokkaido and decimated the local fishery industry, with direct damages totaling approximately \$150 million (Kuroda et al. 2021). In the meantime, neighboring Northeast Asia (NEA; blue box in Fig. 1a; 125–145°E; 30–45°N) experienced extreme terrestrial heat, with regional mean surface air temperature anomalies (SATA) reaching 2.32°C, making the Tokyo 2020 Olympics the hottest Games in history. This spatially concurrent marine and terrestrial heat may cause regionally compounding effects, including synchronous reductions in fishery and agricultural yields and potential impacts on food security (Zscheischler et al. 2020). This spatially compounding heat likely results from a persistent blocking high. It remains poorly understood concerning human influences on the occurrence risk of this compound event. The goal of the present study is to answer this question by assessing whether and to what extent anthropogenic warming has contributed to the occurrence probability of the 2021 NWP concurrent marine and terrestrial summer heat (Perkins-Kirkpatrick et al. 2019; Amaya et al. 2021).

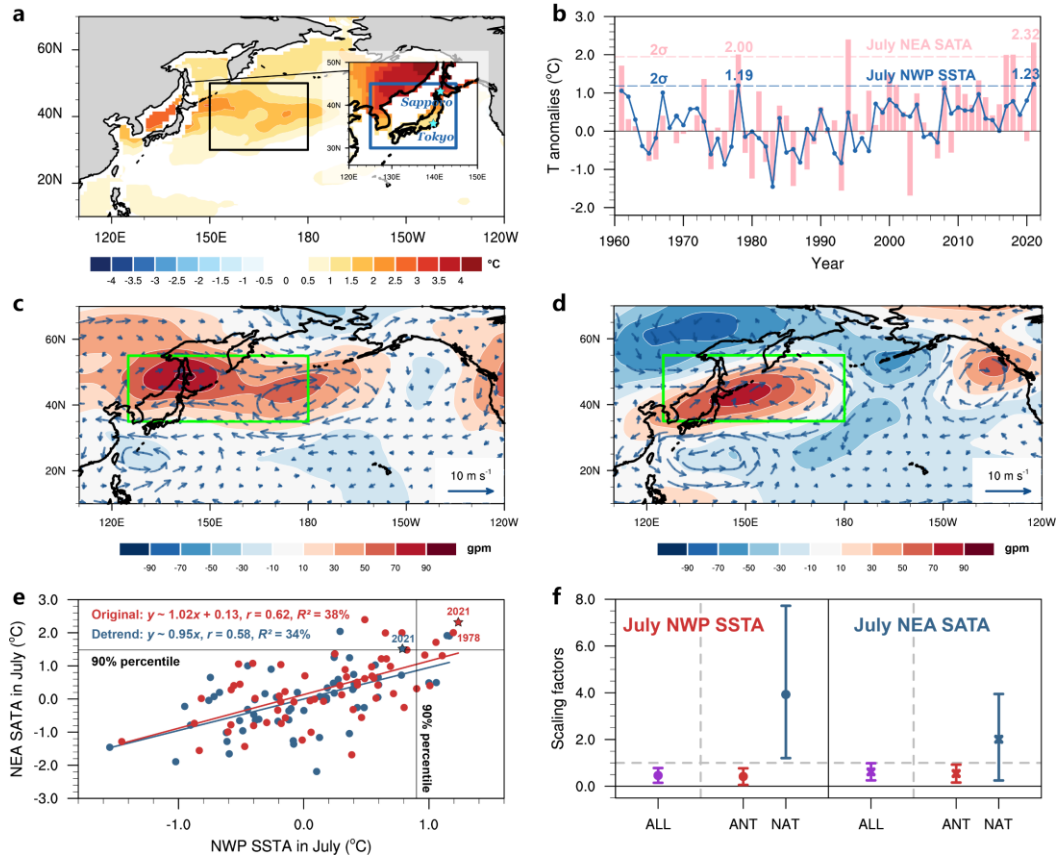


Fig. 1. (a) SSTA (°C) and SSTA (inset; °C) patterns in July 2021. The main hosting cities of the 2020 Tokyo Olympics are marked by pentagrams. The black and blue rectangles encompass the NWP and NEA regions, respectively. (b) The July NWP SSTA (blue solid line; °C) and NEA SSTA (pink bar; °C) during 1961–2021. The 2-σ levels are marked by dashed lines. Values for the years 1978 and 2021 are shown as well. (c) Anomalies of 2021 July 500-hPa geopotential height (with zonal mean removed; shadings; gpm) and 850-hPa horizontal wind (vectors; m s⁻¹) from ERA5. The green rectangle indicates the target circulation region. (d) Same as (c), but for the year 1978. (e) Statistical dependence between July NWP SSTA and NEA SSTA. Red dots indicate the original data, and blue dots the linearly detrended ones. The year 2021 is marked by pentagrams and the 90% percentiles are highlighted. The linear regression model, the Pearson correlation coefficient (r), and the proportion of the variance of y explained by x (R^2) are also shown. (f) The best estimate and 90% confidence interval of the scaling factors (derived from the ROF) for ALL, ANT, and NAT forcings in July NWP SSTA and NEA SSTA.

Data. We focus on July mean temperature anomalies since both marine and terrestrial heat occurred in July 2021. We find modest differences of about 0.1°C exist in July SSTA among different data sets (Fig. S1). To minimize uncertainties, we calculate the ensemble mean of three monthly data sets (HadISST, Rayner et al. 2003; ERSST v5,

Smith et al. 2008; COBESST v2, Hirahara et al. 2014) as the best observational SSTA estimate. We use the monthly gridded Berkeley Earth land-surface temperature (BEST, Rohde et al. 2013) to calculate SATA over terrestrial NEA. We also use monthly 850-hPa horizontal wind and 500-hPa geopotential height data from the ERA5 reanalysis (Hersbach et al. 2020). We focus our analyses on 1961–2021 and the results are generally robust against different choices of studying periods and climate norms.

We use model outputs of monthly SAT, surface temperature, and geopotential heights from the CMIP6 archive to investigate the influences of anthropogenic forcings (ANT; Eyring et al. 2016). To improve the sampling of internal climate variability, we require each model to have at least three ensemble members and 500 years of preindustrial control (pi-CTL) run. Ten models satisfy this criterion, which produce historical simulations until 2014 with all forcings (ALL; hist-All) and until 2020 with natural-only forcings (NAT; hist-Nat), and future projections unfolding along two different Shared Socioeconomic Pathways (SSP2-45 and SSP5-85) (Table S1). Since SSP2-45 forcings were employed in hist-Nat simulations for 2015–2020 (Gillett et al. 2021), we extend the hist-All simulations with corresponding SSP2-45 experiments for this period. All the data are bilinearly interpolated to a $1^\circ \times 1^\circ$ grid from their respective original grids and the results are generally robust against different interpolation methods.

Methods. Accounting for potential biases in the simulated responses to forcings, we first perform calibration analysis using regularized optimal fingerprinting method (ROF; Allen and Stott 2003; Ribes et al. 2013). Briefly, based on a total-least-squares algorithm, this technique regresses the observed change onto the simulated responses to different forcings and accounts for the noise in the model responses associated with internal variability (Note S1). After ensuring the detectability of ANT, we use the ROF-derived regression coefficient (i.e., scaling factor) of ANT to calibrate historical and future ANT signals. We add these observationally-constrained ANT signals to non-overlapping 60-year chunks of unforced series (pi-CTL simulations) to create plausible realizations of NWP SSTA and NEA SATA (Sun et al. 2014). We compare the

constructed evolutions involving anthropogenically-forced warming with the unforced ones to investigate the overall contribution of human influences to the event risk. To reduce uncertainties related to statistical methods, here we use three different approaches to estimate the joint probabilities of occurrence of 2021-like spatially concurrent heat extremes with and without human influences (P_{ANT} and P_{CTL}) by:

I) empirically counting the occurrence of the events with SSTA and SATA exceeding their respective thresholds (i.e., the 1978 event; Figs. 1b, 1e);

II) using a Gaussian copula to model the co-dependence of SSTA and SATA and derive bivariate exceedance probability (Nelsen 2007);

III) using a Gaussian bivariate kernel density estimator (GBKDE; Terrell and Scott 1992).

We compute the probability ratio ($PR=P_{ANT}/P_{CTL}$) and its 5–95% uncertainty range via bootstrapping 1000 times (Efron and Tibshirani 1994).

Results. Both the July 2021 NWP SSTA and NEA SATA are above two standard deviations (σ) and are the first and second warmest since 1961, respectively (Fig. 1b). The mid-latitude lobe of the positive Pacific–Japan teleconnection pattern serves as a common driver of sunny and hot weather over subtropical NWP (Figs. 1c, d; Noh et al. 2021). As a result, the marine and terrestrial heat are significantly spatially related (Fig. 1e). Mean anomalous warm air advection from NEA lands to NWP could strengthen their correlation as well.

The ANT and NAT signals are jointly detectable in the observed SSTA and SATA changes, whilst the scaling factors for NAT exhibit a much larger confidence interval (Fig. 1f). The below-unity scaling factors for ANT indicate an overestimate of the amplitude of simulated regional temperature responses to ANT in models (i.e., ‘hot model’ bias; Hausfather et al. 2022). By altering the ANT signals to best match the observed changes and adding them to the unforced simulations, we produce 154 plausible realizations of the 1961–2020 NWP SSTA and NEA SATA evolutions. The

median σ of the 154 reconstructed SSTA and SATA series are 0.64°C and 0.80°C, close to the observations (0.59°C and 0.97°C). The median Pearson correlation between them is 0.58, consistent with the observed (0.62; Fig. 1e). These results suggest that the simulated series faithfully reproduce the observed variability and statistical dependence between NWP and NEA.

Using the unforced simulations and GBKDE, we estimate the occurrence probability of 2021-like NWP spatially concurrent marine and terrestrial summer heat without human-induced warming to be 0.14% (0.09–0.21%) (Figs. 2a, c; Table 1). Due to the effects of historical anthropogenic warming from 1961 to 2020, the marginal probability distributions of NWP SSTA and NEA SATA shift toward high levels (Fig. 2a). The joint exceedance probability derived from the corresponding plausible realizations is 0.67% (0.53–0.81%) and the associated PR is estimated to be 4.63 (3.21–7.31), which signifies that historical human-induced warming has already led to about a fourfold growth in the risk of 2021-like spatially concurrent heat events (Fig. 2c; Table 1). However, the background warming level around 2021 should be higher than the 1961–2020 average. Thus, we repeat the analysis but add the calibrated anthropogenic warming component over 1991–2050 (centered on 2021) to the unforced data (referred to as ANT-SSP2-45). The estimated PR increases to 32.23 (21.98–51.78), which means current human-induced warming has resulted in approximately a 30-fold increase in the event's occurrence probability (Fig. 2c; Table 1). We consider the observationally-constrained ANT signals over 2041–2100 (centered on 2070) to represent future warming in the second half of the 21st century (Figs. 2b, d). Compared to the current level, future similar events would become approximately 6- and 13-fold more likely under SSP2-45 and SSP5-85, respectively (Table 1). The 2021-like spatially concurrent summer heat would become roughly once-in-4-year and once-in-1.5-year events in these scenarios, respectively. Similar conclusions can be drawn from the other two statistical approaches, albeit with some quantitative differences (Table 1).

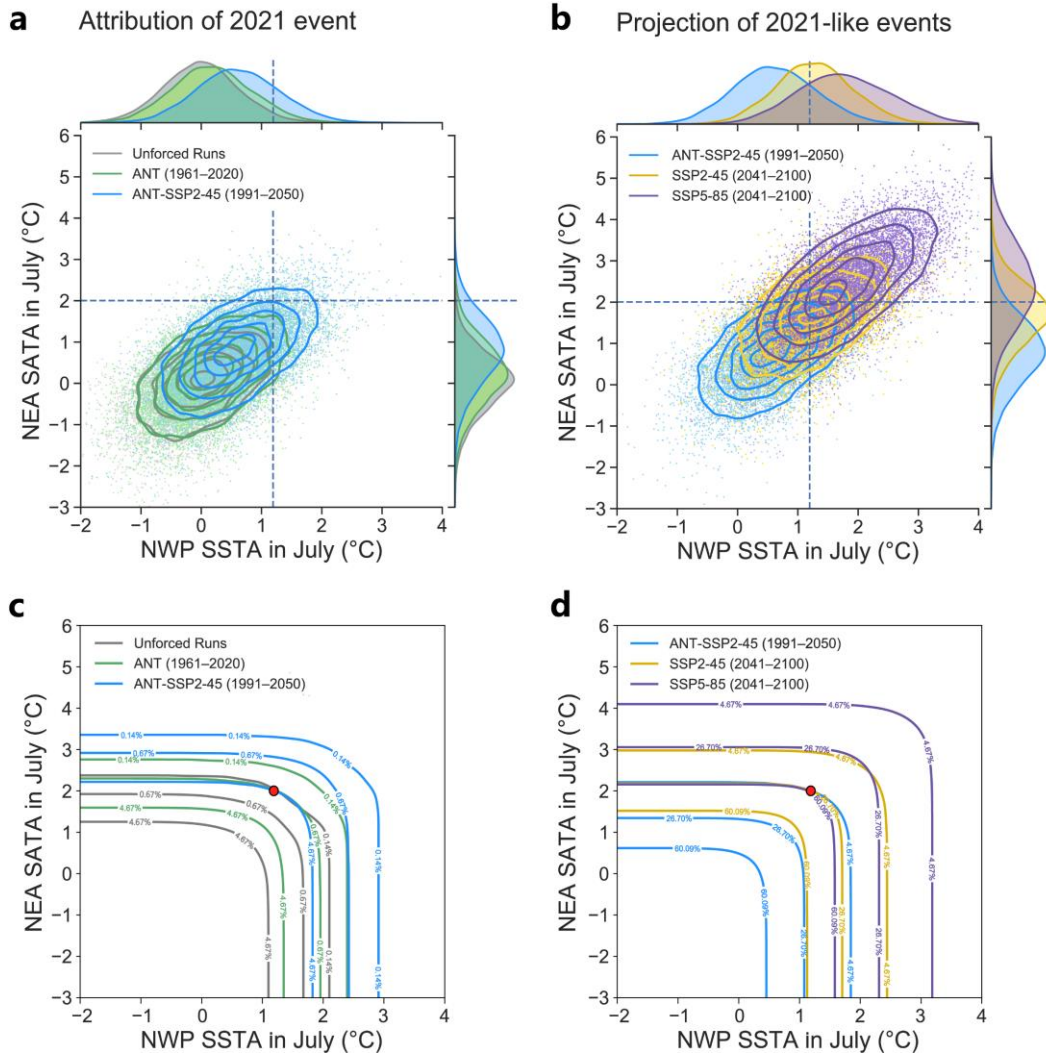


Fig. 2. (a) The marginal and joint probability distributions of July mean NWP SSTA and NEA SATA in the unforced (gray), reconstructed ANT (1961–2020, green) and ANT-SSP2-45 (1991–2050, blue) plausible realizations. The horizontal and vertical dashed lines indicate the NWP SSTA and NEA SATA thresholds (i.e., the 1978 event). From innermost to outermost, the 5th, 25th, 50th, 75th, and 95th percentiles of the distributions (contours) are estimated using a GBKDE. (b) Same as (a), but for ANT-SSP2-45 (1991–2050, blue), and the reconstructed SSP2-45 (gold) and SSP5-85 (purple) plausible realizations over 2041–2100. (c) Joint occurrence risk curves for the unforced (gray), reconstructed ANT (1961–2020, green), and ANT-SSP2-45 (1991–2050, blue) plausible realizations using exceedance probabilities [i.e., $P(X > x, Y > y)$]. The colored numbers embedded in the curves represent joint exceedance probabilities. The red dot marks the joint thresholds. (d) Same as (c), but for ANT-SSP2-45 (1991–2050, blue), and the reconstructed SSP2-45 (gold) and SSP5-85 (purple) plausible realizations over 2041–2100.

Table 1. The marginal (for SSTA and SATA, based on Gaussian fitting) and joint exceedance probability (estimated via three statistical methods) exceeding the observed 2021 thresholds in different reconstructed plausible realizations. The PRs and their corresponding 5–95% ranges are shown as well.

Simulations/PRs	Marginal probability (SSTA)	Marginal probability (SATA)	Joint exceedance probabilities estimated by three different statistical approaches		
			Empirical	Gaussian-Copula	GBKDE
I. Unforced	2.85% (2.67–3.05%)	0.40% (0.36–0.45%)	0.14% (0.08–0.21%)	0.11% (0.09–0.13%)	0.14% (0.09–0.21%)
II. ANT (1961–2020)	6.36% (6.06–6.73%)	1.43% (1.32–1.55%)	0.58% (0.47–0.71%)	0.58% (0.52–0.63%)	0.67% (0.53–0.81%)
PR (II/I)	2.23 (2.05–2.43)	3.57 (3.13–4.10)	4.17 (2.83–7.14)	5.20 (4.78–5.71)	4.63 (3.21–7.31)
III. ANT-SSP2-45 (1991–2050)	20.22% (19.63–20.82%)	7.68% (7.35–8.04%)	4.36% (3.99–4.72%)	4.57% (4.35–4.83%)	4.67% (4.30–5.04%)
PR (III/I)	7.05 (6.55–7.63)	19.28 (17.02–21.82)	31.38 (21.18–55.81)	41.86 (37.76–46.75)	32.23 (21.98–51.77)
IV. SSP2-45 (2041–2100)	55.07% (54.37–55.80%)	33.78% (33.14–33.44%)	25.52% (24.79–26.35%)	25.88% (25.30–26.48%)	26.70% (25.90–27.69%)
PR (IV/III)	2.73 (2.64–2.82)	4.40 (4.19–4.61)	5.86 (5.46–6.34)	5.66 (5.46–5.86)	5.72 (5.32–6.21)
V. SSP5-85 (2041–2100)	77.40% (76.88–77.96%)	65.72% (65.08–66.36%)	58.84% (58.02–59.69%)	59.34% (58.67–60.02%)	60.09% (59.00–61.22%)
PR (V/III)	3.83 (3.72–3.94)	8.54 (8.16–8.93)	13.49 (12.53–14.73)	12.93 (12.38–13.63)	12.88 (11.92–14.12)

The increases in the frequency of 2021-like spatially-compounding heat events may primarily arise from shifts in marginal distribution of NWP SSTA and NEA SATA, with the changing dependence structure contributing little (Figs. 2a, b). This connotes that

their physical linkage via the common anticyclonic pattern has not been and would not be changed by anthropogenic warming. To test this hypothesis, we compute the pattern correlation coefficients (r) between July 2021 500-hPa geopotential height anomalies (with zonal mean removed; Z500') from ERA5 and July Z500' from hist-All (hist-Nat, SSP2-45) simulations during a 60-years period over the target circulation region (green box in Fig. 1c; 125–180°E; 35–55°N). The composite circulations in the analog Z500' patterns that resemble the observed in July 2021 ($r > 0.5$) bear notable similarities among the hist-All, hist-Nat, and SSP2-45 ensembles (Fig. S2a, b, and c). Moreover, there is no significant shift in the frequency of analog Z500' patterns ($r \geq 0.5$) due to historical and future anthropogenic forcings (Fig. S2d). Similar results could be achieved when directly comparing the July Z500' averaged over the target circulation region in the hist-All, hist-Nat, and SSP2-45 simulations (Fig. S2e). In addition, the result is robust against slightly changed target circulation regions and different reanalysis data (figure omitted).

Conclusions. With the aid of CMIP6 multi-model ensemble simulations and optimal fingerprinting detection technique, we find that current human-induced warming has led to about a 30-fold increase in the occurrence probability of a record-breaking spatially concurrent marine and terrestrial summer heat that occurred across the NWP in July 2021. Its occurrence risk in the second half of the 21st century is projected to be at least six times the 2020s level, even under a moderate emission scenario. Results imply that the compounding effects of unprecedented spatially simultaneous heat on agricultural and fishery productions in the NWP and its nearby lands may increase and substantial cuts in emissions are paramount to reduce the risks. This study may shed light on the ongoing efforts attributing less explored yet potentially more impactful spatially compounding events to anthropogenic climate change.

Acknowledgments

This study was supported by the National Natural Science Foundation of China (42025503) and the Strategic Priority Research Programme of the Chinese Academy of Sciences (XDA20020201).

Data Availability

All the data that support the findings are publicly available. The gridded Berkeley Earth Surface Temperature dataset is available at <http://berkeleyearth.org/data>. The HadISST, ERSST v5, and COBESST v2 data sets can be downloaded from their official websites <https://www.metoffice.gov.uk/hadobs/hadisst/>, <https://data.noaa.gov/dataset/dataset/noaa-extended-reconstructed-sea-surface-temperature-ersst-version-5>, and <https://data.noaa.gov/dataset/dataset/cobe-sst2-sea-surface-temperature-and-ice>, respectively. The model outputs in CMIP6 can be accessed at <https://esgf-node.llnl.gov/projects/cmip6/>. The ERA5 reanalysis data can be secured from <https://www.ecmwf.int/en/forecasts/datasets/reanalysis-datasets/era5> on registration.

References

- Allen, M. R., and P. A. Stott, 2003: Estimating signal amplitudes in optimal fingerprinting, part I: theory. *Clim. Dyn.*, **21**, 477–491.
- Amaya, D. J., and Coauthors, 2021: Are long-term changes in mixed layer depth influencing North Pacific marine heatwaves? *Bull. Amer. Meteor. Soc.*, **102**, S59–S66.
- Efron, B., and R. Tibshirani, 1994: An Introduction to the Bootstrap. CRC Press, 456 pp.
- Eyring, V., S. Bony, G. A. Meehl, C. A. Senior, B. Stevens, R. J. Stouffer, and K. E. Taylor, 2016: Overview of the Coupled Model Intercomparison Project Phase 6 (CMIP6) experimental design and organization. *Geosci. Model Dev.*, **9**, 1937–1958.
- Gillett, N. P., and Coauthors, 2021: Constraining human contributions to observed warming since the pre-industrial period. *Nat. Clim. Chang.* **11**, 207–212.

- 229 Hausfather, Z., K. Marvel, G. A. Schmidt, J. W. Nielsen-Gammon, and M. Zelinka, 2022:
230 Climate simulations: recognize the ‘hot model’ problem. *Nature* **605**, 26–29.
- 231 Hersbach, H., and Coauthors, 2020: The ERA5 global reanalysis. *Q. J. R. Meteorol. Soc.*, **146**,
232 1999–2049.
- 233 Hirahara, S., M. Ishii, and Y. Fukuda, 2014: Centennial-scale sea surface temperature analysis
234 and its uncertainty. *J. Clim.*, **27**, 57–75.
- 235 Kuroda, H., and T. Setou, 2021: Extensive marine heatwaves at the sea surface in the
236 northwestern Pacific Ocean in summer. *Remote Sens.*, **13**, 3989.
- 237 Kuroda, H., T. Azumaya, T. Setou, and N. Hasegawa, 2021: Unprecedented outbreak of harmful
238 algae in Pacific coastal waters off southeast Hokkaido, Japan, during late summer 2021
239 after record-breaking marine heatwaves. *J. Mar. Sci. Eng.*, **9**, 1335.
- 240 Nelsen, R. B., 2007: An introduction to copulas. Springer Science & Business Media.
- 241 NOAA National Centers for Environmental Information, State of the Climate: Monthly Global
242 Climate Report for July 2021, published online August 2021, retrieved on May 17, 2022,
243 from <https://www.ncei.noaa.gov/access/monitoring/monthly-report/global/202107>.
- 244 Noh, E., and Coauthors, 2021: The role of the Pacific-Japan pattern in extreme heatwaves over
245 Korea and Japan. *Geophys. Res. Lett.*, **48**, e2021GL093990.
- 246 Perkins-Kirkpatrick, S. E., and Coauthors, 2019: The role of natural variability and
247 anthropogenic climate change in the 2017/18 Tasman Sea marine heatwave. *Bull. Amer.*
248 *Meteor. Soc.*, **100**, S105–S110.
- 249 Rayner, N., and Coauthors, 2003: Global analyses of sea surface temperature, sea ice, and night
250 marine air temperature since the late nineteenth century. *J. Geophys. Res.*, **108**, 4407.
- 251 Ribes, A., S. Planton, and L. Terray, 2013: Application of regularised optimal fingerprinting to
252 attribution. Part I: method, properties and idealised analysis. *Clim. Dyn.*, **41**, 2817–2836.
- 253 Rohde, R., and Coauthors, 2013: A new estimate of the average earth surface land temperature
254 spanning 1753 to 2011. *Geoinfor. & Geostat.: An Overview*, **1**, 1–7.
- 255 Smith, T. M., R. W. Reynolds, T. C. Peterson, and J. Lawrimore, 2008: Improvements to
256 NOAA's historical merged land-ocean surface temperature analysis (1880–2006). *J. Clim.*,
257 **21**, 2283–2296.
- 258 Sun, Y., and Coauthors, 2014: Rapid increase in the risk of extreme summer heat in Eastern
259 China. *Nat. Clim. Chang.*, **4**, 1082–1085.
- 260 Terrell, G. R., and D. W. Scott, 1992: Variable kernel density estimation. *Ann. Stat.*, **20**, 1236–
261 1265.

262 Zscheischler, J., and Coauthors, 2020: A typology of compound weather and climate events.
263 *Nat. Rev. Earth Environ.* **1**, 333–347.